TOPICAL REVIEW

Preparation and Adsorption Properties of Magnetic Composite Microspheres Containing Metal–Organic Double Network Structure

Junfeng Shi[1,2] · Hong Zhang[1,2] · Yue Yu[1,2] · Ming Yan[1,2] · Lingwei Liu[1,2] · Haotong Zhu[1,2] · Yongming Ye[1,2] · Yunhe Zhao[1,2] · Jing Guo[1,2]

Abstract

Acrylamide, sodium alginate and ferroferric oxide were used as raw materials to prepare polyacrylamide/calcium alginate/ferroferric oxide magnetics composite microspheres with metal–organic double network skeleton structure. Chemical structure, thermal stability, crystallization ability, specific surface area and pore structure, surface morphology of the microspheres were characterized by Fourier transform infrared spectroscopy (FTIR), thermogravimetric analyzer (TGA), X-ray diffractometer (XRD), specific surface area analyzer (BET) and scanning electron microscope (SEM). The effects of pH value, temperature, amount of adsorbent and triiron tetroxide on the adsorption of methylene blue (MB) were studied. At the same time, the experiments of reusability were also carried out multiple adsorption/desorption cycles on the adsorption of MB by microspheres. The maximum adsorption capacity was 71.6 mg/g. Adsorption kinetics studies show that the quasi-first-order kinetic model can be better fit the experimental data, and the Freundlich isotherm model fits a good correlation with MB adsorption. In addition, after 5 adsorption/desorption cycles, the removal rate of the adsorbent was maintained at about 94.6%, indicating that it can be reused.

Keywords Polyacrylamide · Sodium alginate · Methylene blue · Adsorbent · Double network

1 Introduction

Modern society currently relies upon the consumption of fossil fuels as the sources of conventional energy. However, their fast depletion has led to serious energy crisis since fossil fuels are limited and exhaustible [1]. The growth and use of renewable energy assets have been involved profusely of research considerations nowadays [2]. Energy and water are the two major issues facing the modern mankind. Providing freshwater requires energy and producing energy uses water [3]. But industries such as leather, paper, plastics, cosmetics and textiles emit large Amounts of wastewater

into the environment. These industrial wastewater contains many dyes. However, most organic dyes have toxic effects on humans and microorganisms, and the molecular structure of these dyes is usually very stable [4–7]. MB, an aromatic heterocyclic compound that is part of a representative contaminant in wastewater, is carcinogenic, teratogenic and mutagenic to humans and difficult to biodegrade. Therefore, the treatment of MB in industrial wastewater has become an urgent problem to be solved [8]. At present, the treatment of dye in wastewater can be generally classified into the following six methods: biological methods, chemical oxidation, flocculation sedimentation, electrolysis, adsorption and photosynthesis degradation [9–18]. Titania (TiO_2) nanofibers are widely exploited due to their unique properties, high oxidative capacity, low cost, as well as extensive applications in environmental cleaning and protection, photocatalysis, photoelectrode, gas sensing, optical coating [19]. Kakarla et al. Prepared TiO_2 @ C nanofiber composites using electrospinning technology, which has excellent photocatalytic performance and recyclability in water purification [20]. But among them, the adsorption method is simple, low in energy consumption and recycling in wastewater treatment, and it

✉ Hong Zhang
752674967@qq.com

✉ Yue Yu
yuyue@dlpu.edu.cn

1 School of Textile & Materials Engineering, Dalian Polytechnic University, Dalian 116034, China

2 Functional Fiber and Composite Materials in Liaoning Province Engineering Research Center, Dalian 116034, China

is an ideal wastewater treatment method [21]. Therefore, the development and utilization of adsorbents is a key factor in adsorption processing. Polyacrylamide (PAM) is a water-soluble linear high molecular polymer obtained by radical polymerization of acrylamide (AM) monomer. PAM microspheres and their composites are used in sewage treatment with good adsorption effects of MB, Cd (II) and Remazone red in sewage [22, 23]. However, the pure PAM gel is inferior in strength, single pollutant removal ability, and poor ability to treat small molecules in wastewater. It is not degradable and non-recyclable. It is easy to cause secondary pollution when it is discharged into nature during the process of treating sewage, which is harmful to animals and plants. The poly (AM-methacrylate) adsorbent prepared by Milosavljevic et al. [24] is used to adsorb Cu^{2+}. When the amount of adsorbent is 300 mg and the pH is 5, the maximum adsorption capacity of the adsorbent for Cu^{2+} reaches 24.05 mg/g, and the adsorption satisfies the Quasi-First-Order kinetic equation. Liu et al. [25] synthesized ATP/poly (AA-AM) (AA: acrylic acid) adsorbent with 35.94 mg/g of Pb^{2+} by reverse suspension polymerization. Li et al. [26] introduced SA into PAM gel network, and prepared SA/PAM hydrogel with semi interpenetrating network structure by free radical solution polymerization. The adsorption mechanism of SA/PAM hydrogel on crystal violet (CV) was analyzed. The results showed that the maximum adsorption capacity of SA/PAM gel to CV molecule reached 13.58 mg/g, which accords with pseudo first order adsorption kinetics model. And the recycling of adsorbent has been confirmed. Our group introduced sodium alginate (SA) into PAM system and designed a PAM/SA microsphere with a double network structure by using continuous inverse emulsion polymerization and ionic coupling. Microspheres which achieve the blending of two substances and prevent the escape of molecules [27]. In order to further solve the secondary environmental pollution caused by difficult to recycle microspheres, we designed and prepared a magnetic composite microsphere containing nano-ferric oxide (Fe_3O_4).

Fe_3O_4 nanoparticles have the advantages of excellent superparamagnetism, high specific surface area, and low toxicity. They are widely used in environmental protection, biomedicine and other fields [28–30]. Moreover, Fe_3O_4 is easily recovered under an external magnetic field [31] and thus has been used as an adsorbent in recent years. The magnetic Fe_3O_4 nanoparticles are introduced into polyacrylamide/calcium alginate (PAM/CA) double network microspheres and the metal–organic framework structure is constructed by the coordination interaction of Fe_3O_4 nanoparticles and hydrogen bonding ligands. The structure can not only synergistically increase the adsorption specific surface area, but also obtain magnetic separation ability for recycling. In this experiment, the "one-pot method" is used to synthesize PAM/CA/Fe_3O_4 magnetic composite microspheres by

emulsion polymerization and ion crosslinking method using AM, Fe_3O_4 and SA as raw materials to prepare adsorbents with high adsorption capacity and magnetic separation. The adsorption performance and mechanism of MB in aqueous solution were examined. The removal rate of the adsorbent was maintained at about 94.6% after 5 adsorption/desorption cycles, indicating that it can be reused. However, because sodium alginate is more expensive, it is difficult to reduce the cost of preparing the adsorbent.

2 Materials and Methods

2.1 Chemicals

SA, food grade, Qingdao Mingyue Seaweed Group Co., Ltd.; AM, analytical pure, Tianjin Guangfu Fine Chemical Research Institute; ammonium persulfate (APS), calcium chloride ($CaCl_2$), cyclohexane, trisodium citrate, analytical grade, Tianjin Kemiou Chemical Reagent Co., Ltd.; N, N-methylenebisacrylamide (MBA), Span60, Tween60, chemically pure, Shanghai Maclean Biochemical Co., Ltd.; anhydrous ethanol, analytically pure, Tianjin Fu Yu Fine Chemical Co., Ltd.; MB, analytical pure, Tianjin Aopusheng Chemical Co., Ltd.; Fe_3O_4, Analytical Pure, Shanghai Maclean Biochemical Co., Ltd. All materials were used as received without any purification.

2.2 Preparation of Adsorbent

100 g of cyclohexane was weighed and added to a 250 mL three-necked flask equipped with a digital high-speed disperser and a reflux condenser. 7.5 g of Span 60 and 2.5 g of Tween 60 were then added to a three-necked flask to prepare an oil phase. In a beaker, 5 g of AM, 0.75 g of MBA, 1 g of trisodium citrate, 1 g of Fe_3O_4 and 1 g of SA were dissolved in 50 mL of deionized water to prepare an aqueous phase. The aqueous phase was slowly added to a three-necked flask containing the prepared oil phase by a propulsion device, and the mixture was continuously stirred for 30 min. Then, 0.25 g of APS was added to a three-necked flask containing a mixture of oil and water phases, stirring was continued for 10 min, and the temperature was raised to 60 °C. After 1 h, a 3% calcium chloride solution was added to the above reaction system, and the reaction was continued for 30 min. The emulsion was demulsified with absolute ethanol and precipitated after centrifugation. The precipitate was further washed 3 times with absolute ethanol, and then with deionized water. It was dried in a freeze dryer for 24 h to obtain black PAM/CA/Fe_3O_4 magnetic composite microspheres. The scheme of the synthesis of magnetic composite microspheres is shown in Fig. 1:
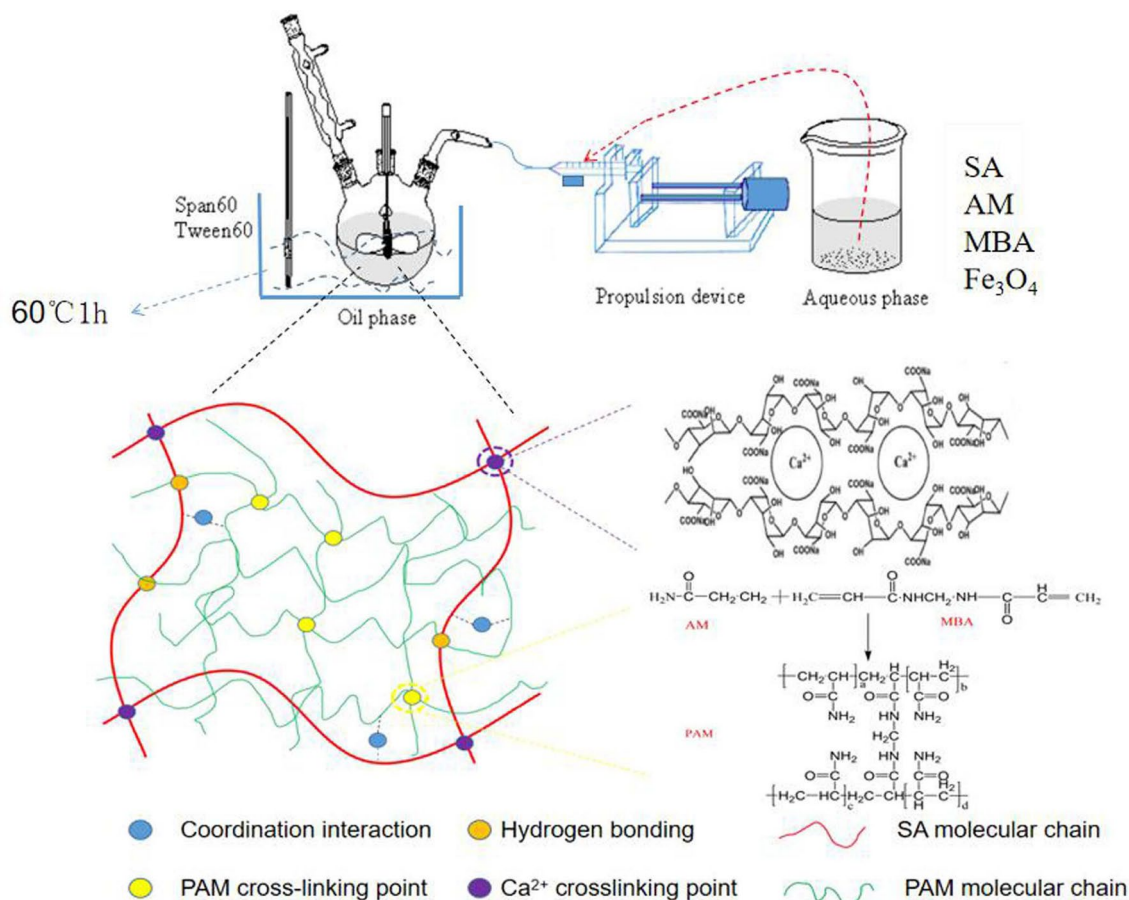
Fig. 1 The scheme of the synthesis of magnetic composite microspheres

2.3 Characterization

Chemical structure: The molecular structure of the microspheres was characterized by Spectrum One-B type Fourier infrared spectrometer. The infrared spectrum was measured by potassium bromide tableting method and the scanning range was 400–4000 cm^{-1}.

Thermal decomposition performance: It was tested by Q50 type thermogravimetric analyzer produced by American TA Company, using nitrogen as protective gas with nitrogen flow rate of 50 mL/min, test temperature range from room temperature to 700 °C at a heating rate of 20 °C/min.

Crystallization performance: It was tested by D/max-3B X-ray diffractometer manufactured by Nippon Science Co., Ltd., with an operating voltage of 40 kV, the scanning range is 5 to 70° at a scanning speed of 5°/min.

Surface morphology and element distribution analysis: The surface morphology and element distribution of PAM/CA/Fe$_3$O$_4$ composite microspheres with different Fe$_3$O$_4$ content were observed by JEOL JSM-6460LV scanning electron microscope manufactured by JEOL.

2.4 Adsorption Experiment on Dyes

0.1 g of the composite microspheres was taken and added to 100 mL of 100 mg/L MB solution at room temperature for 1 h of static adsorption. After adsorption equilibrium, the microspheres were taken out and washed with deionized water and the adsorption capacity was calculated. The absorbance of the supernatant in the beaker was measured by UV/Vis spectrophotometer and converted into the concentration of the dye solution. The adsorption capacity and dye removal rate of PAM/CA/Fe$_3$O$_4$ composite microspheres were calculated using the following formula:

$$q_e = (C_0 - C_e) \times V/M \tag{1}$$

$$r = (C_0 - C_e)/C_0 \times 100\% \tag{2}$$

where q_e is the equilibrium adsorption capacity (mg/g), C_o and C_e are the initial mass concentration and equilibrium mass concentration (mg/L) of MB solution, respectively. V is the total solution volume (L), M is the mass of the adsorbent (g), and r is the removal rate (%).

The washed composite microspheres were transferred to 100 mL of a hydrochloric acid solution with a pH of 3. The composite microspheres were uniformly dispersed in the solution while being desorbed under a water bath condition of 25 °C. After 24 h, the supernatant liquid was taken and UV was used. The visible light spectrophotometer was used to measure the MB concentration in the solution and the desorption rate of the composite microspheres is calculated by the formula (3). After five times of adsorption/desorption cycle, the adsorption capacity of the micrspheres after multiple adsorption/desorption cycles was compared.

$$w = \frac{C_1 \times V}{q_e \times m} \times 100\% \tag{3}$$

where w represents the desorption rate, %; C_1 represents the concentration of the solution after desorption, mg/L; V represents the volume of the solution, L; q_e is the adsorption capacity of the last adsorption, mg/g; m represents the adsorbent quality, g.

3 Results and Discussion

3.1 FTIR of PAM/CA/Fe₃O₄ Hybrid Adsorbent

Figure 2 shows the infrared spectrum of the PAM, CA, Fe₃O₄ and PAM/CA/Fe₃O₄ microspheres before and after adsorption of methylene blue. On the spectrum of PAM, the –NH₂ characteristic absorption peak is at 3469 cm⁻¹, 2930 cm⁻¹ and 2865 cm⁻¹ are the antisymmetric and symmetric stretching vibration absorption peaks of –CH₂, and
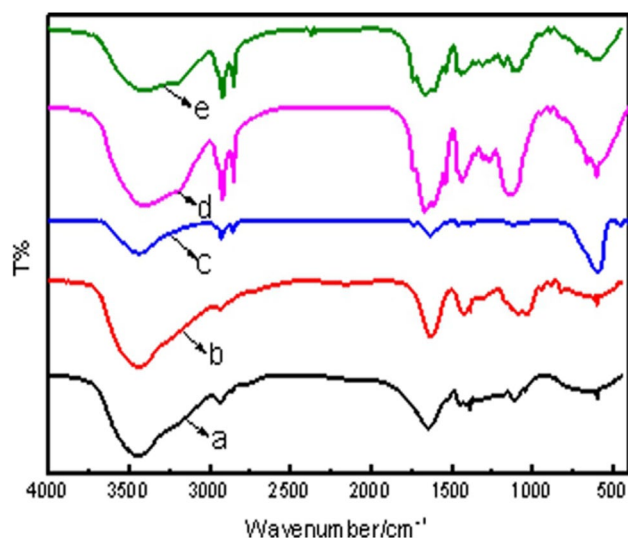

Fig. 2 Infrared spectrum of different samples (*a*) PAM, (*b*) CA, (*c*) Fe₃O₄, (*d*) PAM/CA/Fe₃O₄ microsphere before adsorption, (*e*) PAM/CA/Fe₃O₄ microsphere before adsorption)

the stretching vibration peaks of –CN is at 1181 cm⁻¹ and 1108 cm⁻¹. The obvious characteristic absorption peaks at 3444 and 1636 cm⁻¹ of the spectrum of CA are characteristic peaks of –OH tensile vibration and bending vibration, and –CO absorption peak is at 1030 cm⁻¹. The stretching vibration absorption peak of Fe–O is at 586 cm⁻¹ of the spectrum of Fe₃O₄ [32]. The characteristic peaks of these components are reflected on the spectrum of PAM/CA/Fe₃O₄. On PAM/CA/Fe₃O₄ spectrum, a strong absorption peak appeared at 3410 cm⁻¹ and the width of the peak increased compared with the PAM and CA components, which was the result of the superposition of –NH₂ and –OH peaks. The strong absorption peak at 2930 cm⁻¹ is the result of the superposition of the -CH₂ phase. PAM has a –C=O peak at 1642 cm⁻¹, CA also has a –C=O peak at 1630 cm⁻¹, on PAM/CA/Fe₃O₄ spectrum, the strong absorption peak at 1660 cm⁻¹ is the result of the superposition of the –C=O phase of PAM and CA. Due to the hydrogen bonding between the –NH₂ of PAM and the –OH of SA, the peaks at 3649 and 3444 cm⁻¹ are shifted to 3410 cm⁻¹. Due to the coordination interaction between Fe₃O₄ and PAM or CA, the wavenumbers of the peaks at 1108 and 1030 cm⁻¹ are significantly shifted to high frequencies. Comparing the infrared spectra of PAM/CA/Fe₃O₄ before and after adsorption, the peak at 3410 cm⁻¹ after adsorption was significantly weakened by the hydrogen bonding of –NH₂ and –OH with MB and the MB aromatic ring appeared at 1500 and 1219 cm⁻¹. The characteristic stretching vibration absorption peak indicates that the MB is successfully adsorbed, that is, the infrared result proves that the PAM/CA/Fe₃O₄ composite microsphere with the metal–organic double network skeleton structure is successfully constructed and the MB is successfully adsorbed.

3.2 Thermogravimetric Analysis of PAM/CA/Fe₃O₄ Composite Microspheres

As shown in Fig. 3a and b, the TGA and DTA curves of different Fe₃O₄ content magnetic composite microspheres. In the temperature variation range, the thermal decomposition curve of PAM/CA/Fe₃O₄ magnetic composite microspheres can be roughly divided into four stages. The first stage at 30–200 °C represents the volatilization and small amount of bound water in the composite microspheres. The maximum weight loss rate occurs at 100 °C. The water content of magnetic microspheres reduced due to the addition of Fe₃O₄, because the increase of Fe₃O₄ content reduces the proportion of SA and PAM, resulting in a decrease in water content. The second stage of 200–300 °C represents the decomposition of SA. Near 200 °C, the glycosidic bond of SA begins to break and the fracture becomes severe at 250 °C and the decomposition rate is the fastest. Due to the coordination interaction between the hydroxyl group on the SA and the nano-Fe₃O₄, the decomposition temperature of the SA is increased. As
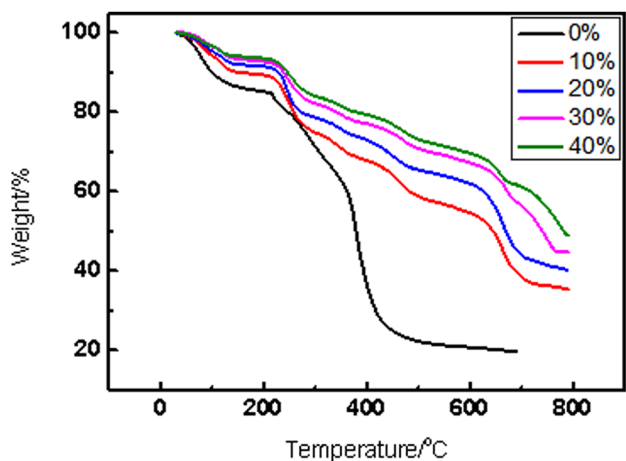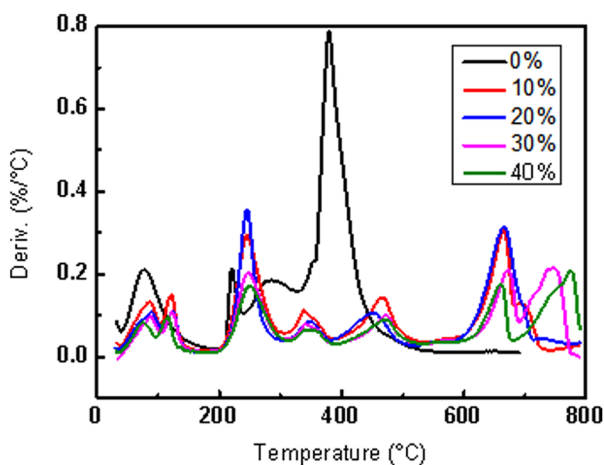
(a) TG curves of different Fe_3O_4 content PAM/CA/Fe_3O_4 microspheres

(b) DTG curves of different Fe_3O_4 content PAM/CA/Fe_3O_4 microspheres

Fig. 3 TG and DTG curves of magnetic composite microspheres with different Fe_3O_4 content. **a** TG curves of different Fe_3O_4 content PAM/CA/Fe_3O_4 microspheres. **b** DTG curves of different Fe_3O_4 content PAM/CA/Fe_3O_4 microspheres

the Fe_3O_4 increases, the decomposition temperature of the SA gradually increases and the heat loss decreases. The third stage at 300–380 °C represents the decomposition of trisodium citrate and the decomposition of low molecular weight PAM. In this temperature range, PAM initiates imidization reaction intermolecularly and intramolecularly, releasing H_2O, NH_3 and CO_2 product. The main decomposition temperature range of PAM is about 380–520 °C. At this time, the PAM molecular chain begins to break. There is a strong interaction between the amide group on the PAM and the nano-Fe_3O_4. The coordination interaction between the ligand and Fe is the main reason for the formation of the metal–organic framework network structure and the decomposition temperature of some PAM is raised to 520 °C, and as the Fe_3O_4 content increases, this decomposition temperature gradually shifts toward high temperature, showing more difficult to degrade.
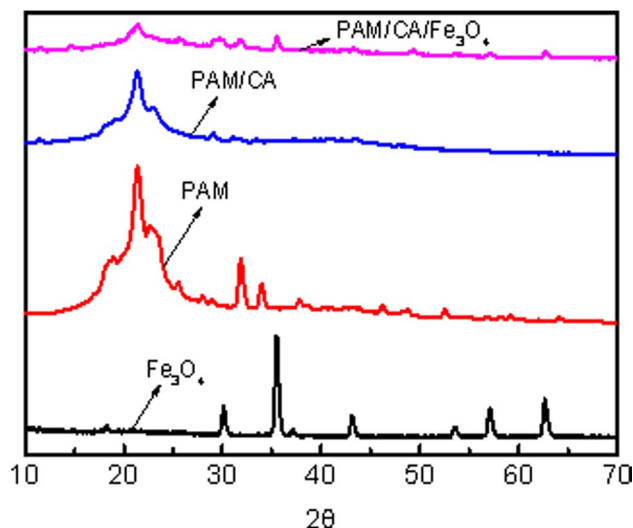

Fig. 4 The XRD spectra of different samples

3.3 Crystallization Analysis of PAM/CA/Fe_3O_4 Composite Microspheres

At a 2θ value of 21°, it is a characteristic peak of PAM. The characteristic absorption peaks of Fe_3O_4 at the 2θ values of 18.26°, 30.1°, 35.38°, 43.06°, 53.5°, 57.04° and 62.6° correspond to the (111), (220), (311), (400), (422), (511) and (440) crystal faces of Fe_3O_4 (JCPDS No. 19-0629), indicating that Fe_3O_4 is a face-centered cubic crystal structure [33]. There is not obvious diffraction peaks after 21° in PAM/CA. This is because SA molecules contain a large amount of hydroxyl groups and carboxyl groups. The steric hindrance of the large group and the interaction between the groups limit the movement of the molecular chain and the SA molecular chain is rigid. This rigid molecular chain is introduced into the flexible network of PAM, which makes the original movement ability much stronger. The movement of the PAM molecular chain is limited. The hydrogen bond interaction between CA and PAM destroys the original molecular orientation of PAM, which makes the arrangement of molecular chains more messy, crystals are blocked, resulting in a decrease in crystallinity. The characteristic peak of Fe_3O_4 can be clearly observed on the PAM/CA/Fe_3O_4 curve, indicating that Fe_3O_4 is successfully blended. Moreover, the diffraction peak of PAM/CA/Fe_3O_4 is weaker than that of other samples due to the electrostatic action of Fe_3O_4 and PAM, the crystallinity is lowered and the diffraction peak is weak (Fig. 4).

3.4 Surface Morphology and Element Distribution Analysis of PAM/CA/Fe₃O₄ Composite Microspheres

Figure 5 is an electron micrograph of microspheres with different nano-Fe₃O₄ content at 1000 times and Fig. 6 was a distribution of Fe elements on the surface of the microspheres. It could be seen from Fig. 5 that when Fe₃O₄ was not added, the prepared composite microspheres were spherical in shape with a smooth surface and no agglomeration occurs between the balls and the balls. After the addition of Fe₃O₄, the surface structure of the composite microspheres was loose and the strip-shaped fibrous structure extends from the inside in a divergent form, forming a structure similar to "sea urchin". With the increased of Fe₃O₄ content, the fibrous structure was thickened and coarsened, and then gathered together to form a strip. Combined with the results of the adsorption experiments, this dense fibrous structure was advantageous

for adsorption because its presence increased the specific surface area of the microspheres.

From the distribution map of iron element (Fig. 6), it could be known that the Fe element was uniformly distributed inside the composite microspheres and the dispersibility was also good. There is no large aggregate, and the uniformity of magnetic composite microspheres is good.

3.5 Analysis of Specific Surface Area and Pore Structure of PAM/CA/Fe3O4 Composite Microspheres

Figure 7a is the nitrogen adsorption–desorption isotherm of the microspheres, and (b) is the pore size distribution curve of the microspheres. The adsorption–desorption isotherm exhibits a typical Langmuir type IV. In the range of relative pressure p/p0 < 0.5, the N_2 adsorption of PAM/CA/Fe₃O₄ magnetic composite microspheres with 20% Fe₃O₄ growed very slowly with the increase of pressure and the isotherm was relatively flat. According to the Kelvin formula,

(a) PAM/CA microspheres   **(b)** 10% composite microspheres   **(c)** 20% composite microspheres

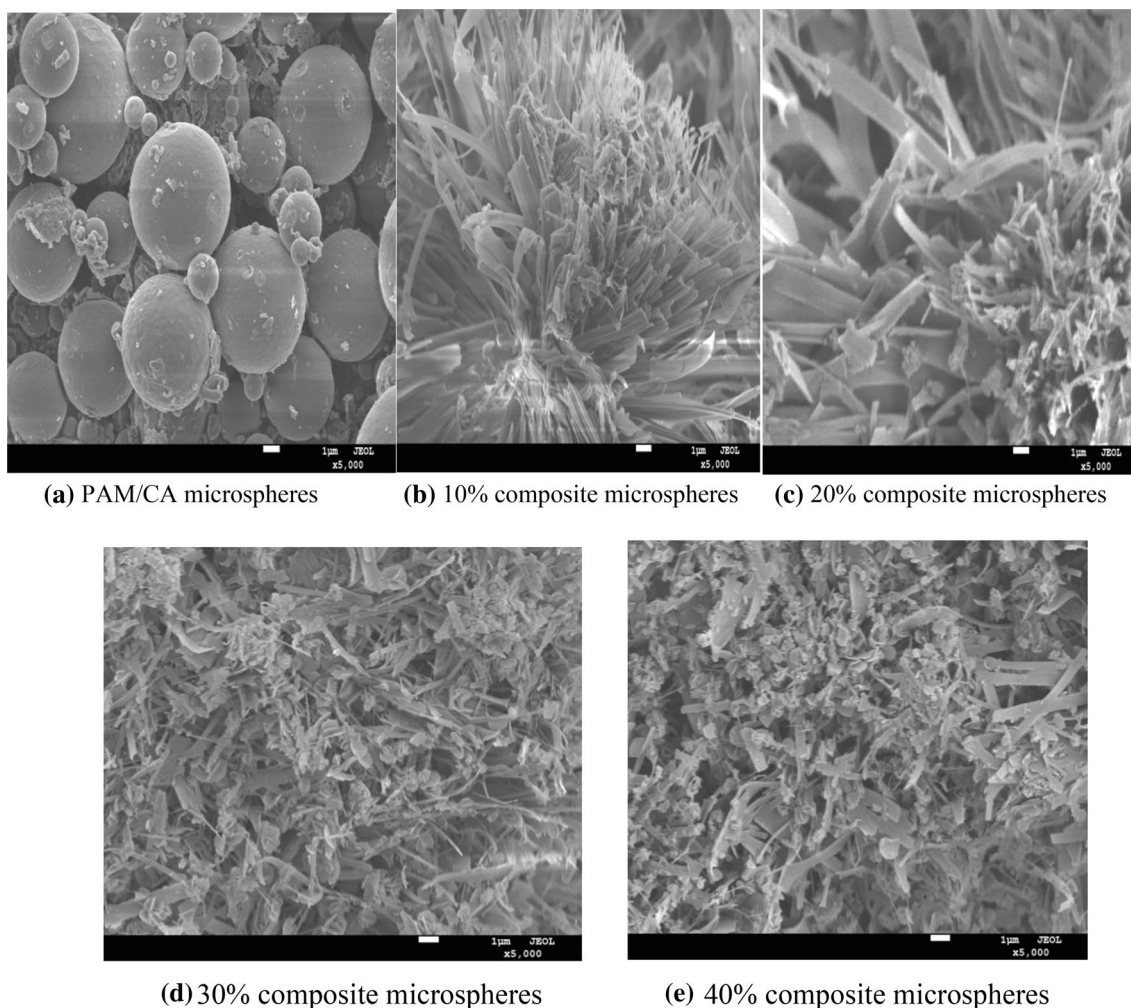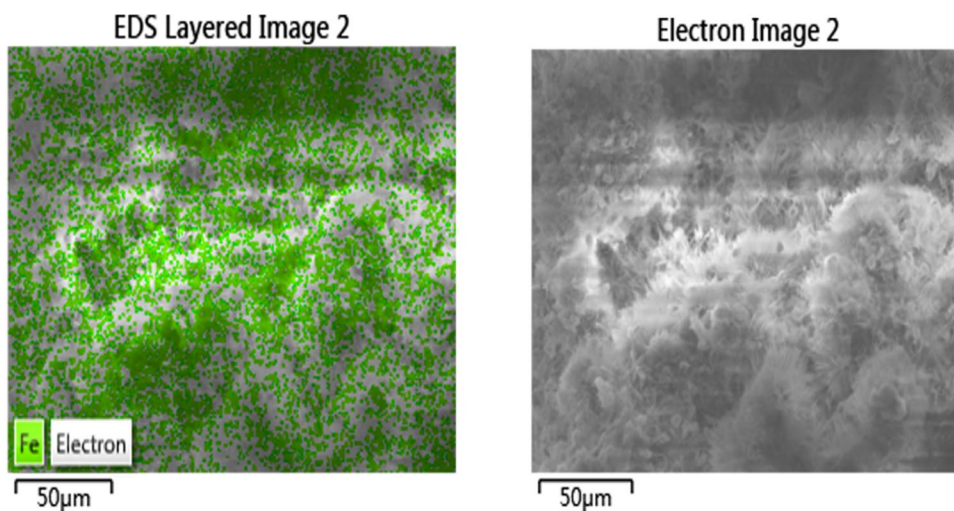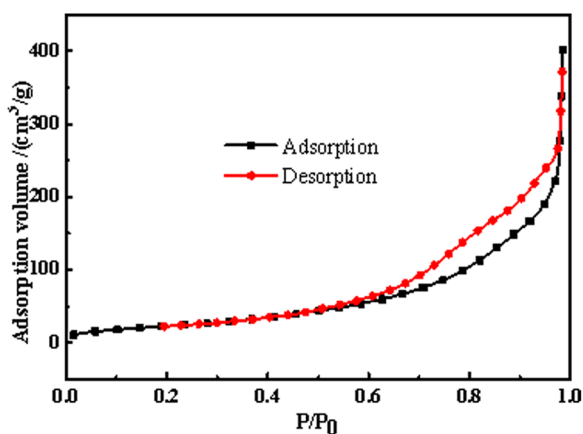**(d)** 30% composite microspheres   **(e)** 40% composite microspheres

Fig. 5 Scanning electron micrographs at 5000 times of magnetic composite microspheres with different Fe₃O₄ content
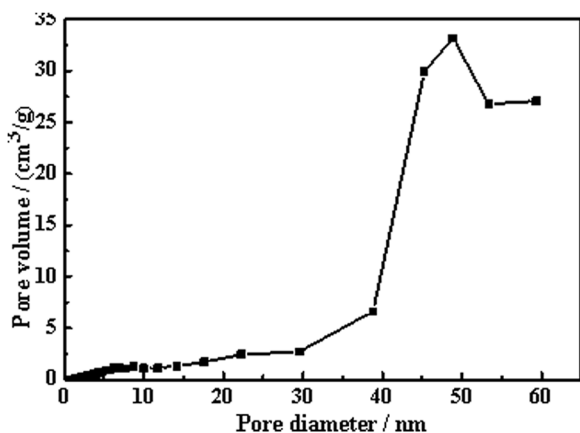
Fig. 6 Distribution of iron elements in PAM/CA/Fe$_3$O$_4$ magnetic composite microspheres containing 20% Fe$_3$O$_4$. **a** EDS image of PAM/CA/Fe$_3$O$_4$ magnetic composite microspheres containing 20% Fe$_3$O$_4$. **b** SEM image of PAM/CA/Fe$_3$O$_4$ magnetic composite microspheres containing 20% Fe$_3$O$_4$

(a) EDS image of PAM/CA/Fe$_3$O$_4$ magnetic composite microspheres containing 20% Fe$_3$O$_4$

(b) SEM image of PAM/CA/Fe$_3$O$_4$ magnetic composite microspheres containing 20% Fe$_3$O$_4$

(a) Adsorption-desorption isotherms of PAM/CA/Fe$_3$O$_4$ magnetic microspheres

(b) Pore size distribution curve of PAM/CA/Fe$_3$O$_4$ magnetic composite microspheres

Fig. 7 N$_2$ adsorption–desorption isotherm and pore size distribution curve of PAM/CA/Fe$_3$O$_4$ magnetic composite microspheres with 20% Fe$_3$O$_4$. **a** Adsorption–desorption isotherms of PAM/CA/Fe$_3$O$_4$ magnetic microspheres. **b** Pore size distribution curve of PAM/CA/Fe$_3$O$_4$ magnetic composite microspheres

when the pore radius was less than 1.5 nm that no capillary condensation occured. So the adsorption amount in the low pressure region was small, and there was no obvious inflection point. The adsorption curve was close to the desorption curve. When the relative pressure p/p0 > 0.5, the adsorption amount increased sharply with the increase of pressure, the desorption curve began to separate from the adsorption curve, a hysteresis occured, and a type IV hysteresis loop appeared. Due to the presence of a certain amount of mesopores and a large pore structure in the sample itself, capillary aggregation occured during the adsorption process, mesopores were filled with condensed N$_2$ molecules. The capillary condensation was carried out on the liquid surface of the annular adsorption membrane on the pore wall, while the desorption was started from the spherical meniscus surface of the orifice, so that the adsorption and desorption isotherms did not coincide, forming a hysteresis loop. The specific surface area of the PAM/CA/Fe$_3$O$_4$ composite microspheres measured by the BET multilayer gas adsorption method was 230 m^2/g.

From the pore size distribution curve, the pore size of the sample was mainly distributed in the range of 40–60 nm and there was a higher peak at 49 nm, which indicating that the pore of this pore diameter accounted for the largest proportion in the sample. The pore size distribution curve of the sample was narrow and the pore size distribution was relatively concentrated. The sample pore size was mainly macropores and mesopores with an average pore diameter of 50 nm. The specific surface area of PAM/CA composite microspheres is 35.56 m^2/g and the average pore diameter of PAM/CA composite microspheres is 11.5 nm in the reported literature [34]. The specific surface area and average pore size of microspheres after adding Fe$_3$O$_4$ have

been greatly improved. It can be explained for two reasons. The mesopores on the sample surface is due to the double network interlocking formed by the entanglement of the PAM and CA molecular chains, resulting in the formation of a three-dimensional mesh structure. On the other hand, the size of the mesh changes due to the addition of Fe_3O_4. The metal–organic double-mesh structure was constituted by the strong coordination interaction between Fe_3O_4 and CA and PAM, which hindering the arrangement of Fe_3O_4 particles, resulting in a radial growth of urchin-like crystal structure between the double grids. According to the BJH theoretical model, the total pore volume of BJH adsorption of PAM/CA/Fe_3O_4 magnetic composite microspheres was 4.9060×10^7 cc/g.

3.6 Analysis of Adsorption Properties of PAM/CA/Fe_3O_4 Composite Microspheres

3.6.1 pH of Dye Solution on Adsorption Performance

The ability of the microspheres to adsorb MB at different pH was examined as shown in Fig. 8. It could be seen that with the increase of pH value, the adsorption capacity of microspheres to MB increases first and then decreases, and the maximum adsorption capacity appears at pH 7. The adsorption of MB dye was driven by the dissociation of hydrogen atoms from the surface of the composite microspheres and nitrogen atoms on the MB to form the hydrogen bonding between N and H. At low pH, the concentration of hydrogen ions in dye solution was large and the activity was high, which would firstly bind to the nitrogen atom of MB and affect the hydrogen bond between the hydrogen atoms on the surface of the microsphere. The free hydrogen

ions in dye solution could also combine with Fe_3O_4 on the surface of the composite microspheres and make Fe_3O_4 protonated, making the adsorption to methylene blue weak, that resulting in lower adsorption capacity. When the pH value gradually increases, the content of free hydrogen ions in the solution will decrease, and the competition with the hydrogen atoms on the surface of the microspheres will weaken, so the adsorption capacity will increase. When the pH was greater than 7, the solution became alkaline, the content of hydroxide would increase, the competitiveness between nitrogen and hydrogen ions would decrease, and the binding force with hydroxide would enhanced, which would weaken the attraction between MB and the binding sites on the surface of the microspheres, thus reducing the adsorption performance.

3.6.2 Solution Temperature on Adsorption Performance

Figure 9 shows the change in the amount of MB adsorbed by PAM/CA/Fe_3O_4 magnetic composite microspheres at different temperatures. It could be seen that when the temperature was gradually increased from 25 to 65 °C, the adsorption capacity was gradually decreased. In the interval of 25–55 °C, the decline was larger that showing a trend of rapid decline. Between 55–65 °C, the downward trend was slowing down. The adsorption of MB dye by magnetic composite microspheres mainly relies on the large specific surface area for physical adsorption. At lower temperature, the adsorption of MB by magnetic composite microspheres was stronger and the removal rate of dye was higher. When the temperature rised, it accelerated the random movement of the MB molecules and destroyed part of the gravitational force, which increased the possibility of desorption.
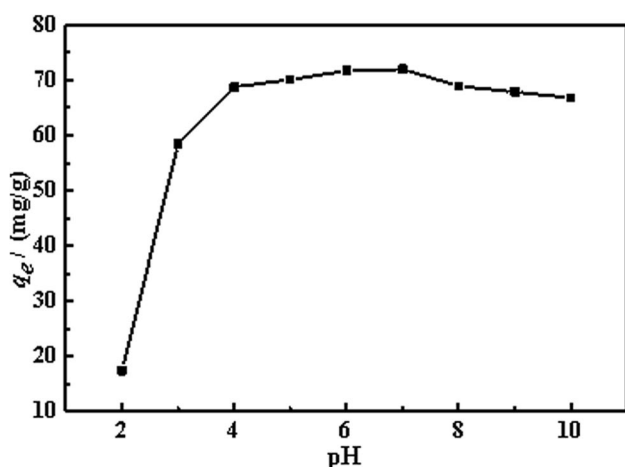

Fig. 8 Adsorption capacity of PAM/CA/Fe_3O_4 composite microspheres at different pH
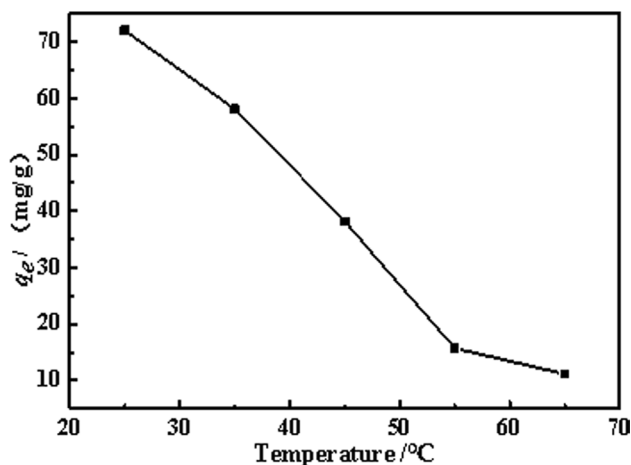

Fig. 9 Adsorption capacity of PAM/CA/Fe_3O_4 composite microspheres at different temperatures
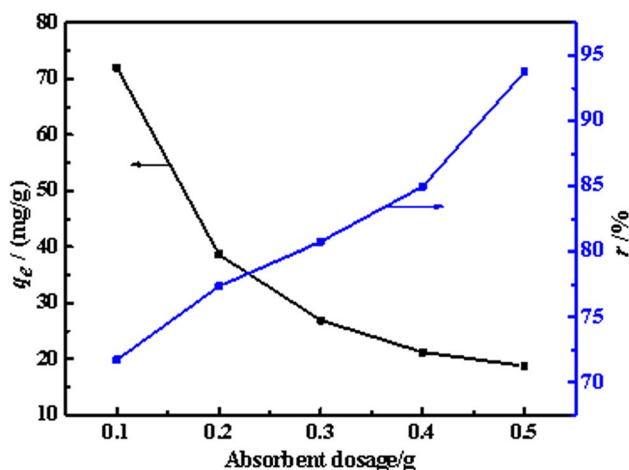
Fig. 10 Effect of different PAM/CA/Fe$_3$O$_4$ composite microspheres dosage on per unit mass adsorption capacity and dye removal rate

Fig. 11 Adsorption capacity of composite microspheres with different Fe$_3$O$_4$ content

Competition between adsorption and desorption progressed, reducing the amount of adsorption.

3.6.3 Adsorbent Dosage on Adsorption Performance

In order to investigate the effect of adsorbent dosage on the adsorption of MB dye by PAM/CA/Fe$_3$O$_4$ magnetic composite microspheres, 0.1–0.5 g adsorbent was used to adsorb the dye solution with the same initial concentration and the results were shown in Fig. 10. It could be seen from the figure that as the amount of adsorbent increases, the per unit mass adsorption capacity of adsorbent decreased but the total removal rate of dyes was gradually increased. The more PAM/CA/Fe$_3$O$_4$ composite microspheres were added, the more active sites were adsorbed. In the case of a certain MB content in water, the amount of MB adsorbed increased that resulting in an increase in removal rate. As the dosage of PAM/CA/Fe$_3$O$_4$ composite microspheres increased, the limited area bound to MB increased. However, the limited area in which the per unit microsphere adsorbent combined with MB was reduced, so that the per unit mass adsorption capacity of the adsorbent was lowered.

3.7 Fe$_3$O$_4$ Content on Adsorption Properties

The difference in the content of Fe$_3$O$_4$ directly caused the difference in adsorption and the result was shown in Fig. 11. It could be seen that as the content of Fe$_3$O$_4$ increased, the adsorption capacity of MB decreased first, then increased, and then decreased. When Fe$_3$O$_4$ was introduced into the system, the specific gravity of PAM and SA
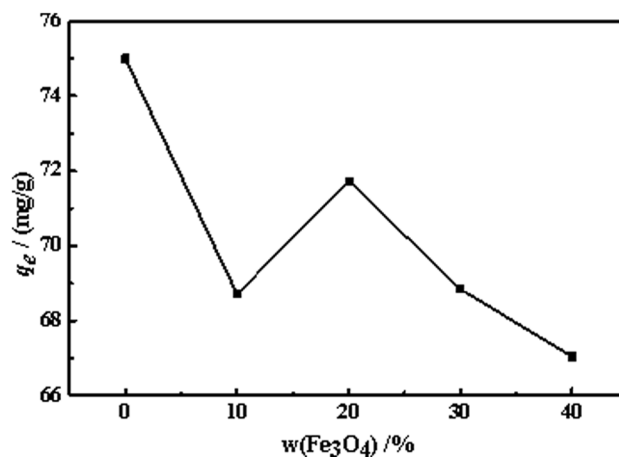
was decreased, which resulting in a decrease in adsorption sites, and thus the adsorption capacity of the composite microspheres for dyes was decreased. When the content of Fe$_3$O$_4$ continues to increase, PAM and SA containing ligands would adsorb with Fe atoms on Fe$_3$O$_4$ due to coordination interaction, and a special metal–organic skeleton structure would be formed. It would greatly increase the pore structure of the microspheres and increased the specific surface area of the microspheres, thereby improving the adsorption performance. However, when the content of Fe$_3$O$_4$ in the system was further increased, the proportion of the skeleton structure in the metal–organic framework structure was reduced, resulting in a decrease in the stability of the skeleton. Moreover, the more Fe$_3$O$_4$ content was, the less stable the microsphere was, which leading to the collapse of the structure. The collapse of microstructure blocked the pore structure inside the microsphere, resulting in the decrease of specific surface area and adsorption capacity. During the experiment, it was found that, except for the component with Fe$_3$O$_4$ added in an amount of 20%, the remaining groups were slightly turbid when adsorbing the MB solution with some fine particles floating in the solution, which made it difficult to recycle and reuse the adsorbent. Therefore, the performance of PAM/CA/Fe$_3$O$_4$ magnetic composite microspheres was the best when the addition amount of Fe$_3$O$_4$ was 20%.

Figure 12 shows a macroscopic picture of magnetic composite microspheres with the optimum addition amount of Fe$_3$O$_4$ before and after adsorption of MB. The color difference is obvious as methylene blue dye was immobilized in the microspheres.

Fig. 12 Macroscopic picture of **a** before and **b** after adsorption of MB with 20% Fe_3O_4 composite microspheres
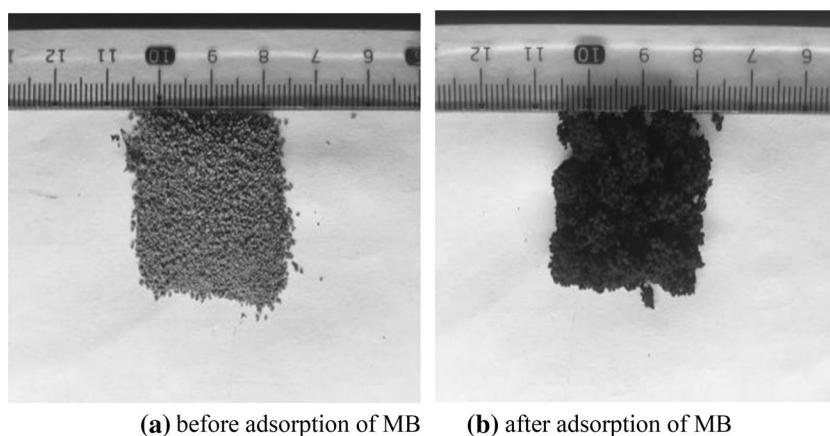
(a) before adsorption of MB   **(b)** after adsorption of MB

Table 1 compared the adsorption of MB by adsorbents prepared by other research groups. It could be clearly seen from the table that the maximum adsorption capacity of the magnetic microspheres of the subject to the methylene blue dye was 71.6 mg/g, which was much higher than most of the reported adsorbents. However, there were still some gaps compared to the maximum adsorption capacity of some other adsorbents. In this paper, the structure of metal–organic double network was constructed by the coordination interaction between metal particles and organic groups. Magnetic particles were introduced to facilitate separation and recycling.

3.8 Recycling of PAM/CA/Fe₃O₄ Composite Microsphere Adsorbent

Figure 13 is a histogram of the adsorption–desorption cycle of PAM/CA/Fe_3O_4 magnetic composite microspheres. It could be seen that as the number of cycles increases, the

adsorption capacity and desorption rate of the composite microspheres increased and then decreased. The main reason was that after the first adsorption, the microspheres were desorbed with a higher concentration of hydrochloric acid solution, and a large amount of hydrogen ions in the solution remove impurities inside the microspheres, opening the pore structure in the microspheres and increasing the pore structure and the specific surface area. Desorption will purify the surface of the microspheres, exposing more adsorption sites inside, which is not only beneficial to the entry of MB molecules, but also the dye molecules are more easily replaced during desorption, so the adsorption capacity and desorption rate will gradually rise. After several adsorption–desorption cycles, multiple acid treatments will destroy the surface structure of the microspheres, cause the collapse of the pores and reduce the specific surface area of the microspheres, making both adsorption and desorption difficult, so the adsorption capacity and the desorption rate have dropped. After four adsorption–desorption cycles, the adsorption of MB dyes by PAM/CA/Fe_3O_4 magnetic composite microspheres remained at a high level with good recyclability.

Figure 14 is a picture of the solution without adding external magnetic force (a) and adding external magnetic force (b) after the microspheres adsorbed MB. It could be clearly seen from the figure that the uniform precipitation of the microspheres in the solution with the added magnet was at the bottom of the conical flask while the liquid surface remains somewhat floating without adding external magnetic force. After the magnet was added, the microspheres rapidly migrate to the magnetic pole and enrich. It was indicated that the magnetic adsorbent PAM/CA/Fe_3O_4 could be separated from the solution by the external magnetic field,

Table 1 Comparison of adsorption of methylene blue dyes by different adsorbents

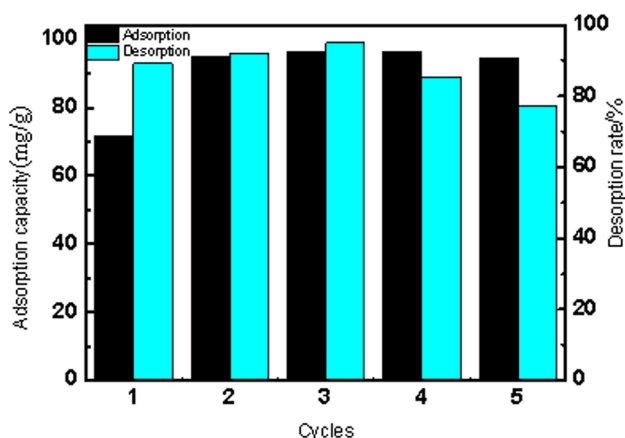| Adsorbents	Dye	Adsorption capacity (mg/g)	Literature
Bamboo leaf powder	MB	46.7	[35]
polyacrylamide/sodiumalginate	MB	75.0	[36]
CoFe₂O₄/MWCNT	MB	14.3	[37]
Carboxymethyl chitosan/polyurethane	MB	24.2	[38]
Magnetic chitosan/diatomaceous earth	MB	76.1	[39]
Grapefruit skin	MB	16.9	[40]
Activated carbon/cellulose	MB	103.66	[41]
Carbonized watermelon rind	MB	200	[42]
Corn stalks	MB	129	[43]
This article	MB	71.6	

Fig. 13 Adsorption capacity and desorption rate of PAM/CA/Fe$_3$O$_4$ composite microspheres with 20% Fe$_3$O$_4$

thereby reducing the loss of the adsorbent and avoiding secondary pollution.

3.9 Adsorption Isotherms of PAM/CA/Fe$_3$O$_4$ Composite Microspheres

The isotherms of adsorption of methylene blue on PAM/CA/Fe$_3$O$_4$ composite microspheres were fitted by Langmuir and Freundlich adsorption thermodynamic models, and the parameters obtained by fitting the two models were compared. The degree of agreement between the two models was investigated. The equation for the model is as follows:

$$q_e = \frac{q_m b C_e}{1 + b C_e} \tag{4}$$

$$q_e = K_f C_e^{1/n} \tag{5}$$

C_e in the formula represents the equilibrium concentration of MB in the solution, mg/L; q_e represents the adsorption capacity of the adsorbent, mg/g; q_m is the maximum adsorption capacity of the adsorbent to the MB dye, mg/g; b is the Langmuir coefficient, L/mg; K_f and n are Freundlich constants.

Figure 15 is an adsorption isotherm fitting curve of adsorption of MB by PAM/CA/Fe$_3$O$_4$ magnetic composite microspheres. It could be seen from Table 2 that the Freundlich correlation coefficient R^2 was higher than that of Langmuir at different temperatures, indicating that the PAM/CA/Fe$_3$O$_4$ magnetic composite microspheres were more in line with the Freundlich isotherm. The Freundlich isotherm model indicates that the adsorption system was multilayer reversible adsorption process that occurs freely on non-porous solid surfaces or macroporous solids [44]. In addition, the correlation coefficient R^2 of the two adsorption isotherms was greater than 0.9, indicating that the adsorption process may be a complex process involving both physical adsorption and chemical adsorption which belongs to multilayer adsorption [45]. The maximum adsorption amount calculated by Langmuir was 749.955 mg/g.

3.10 Adsorption Kinetics of PAM/CA/Fe$_3$O$_4$ Composite Microspheres

The adsorption kinetic curves of PAM/CA/Fe$_3$O$_4$ magnetic composite microspheres were fitted by quasi-first-order and quasi-second-order adsorption kinetics models. The agreement between the two models was investigated. The equation is as follows:

$$\ln(q_e - q_t) = \ln(q_e) - K_1 t \tag{6}$$

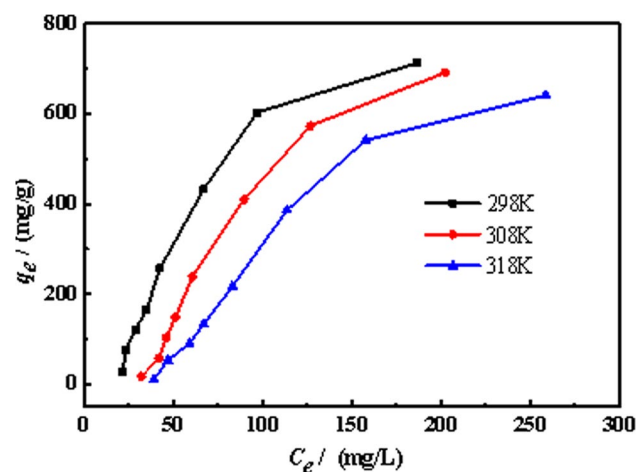**Fig. 14** After the adsorption of MB, the solution without adding external magnetic force (**a**) and adding external magnetic force (**b**)
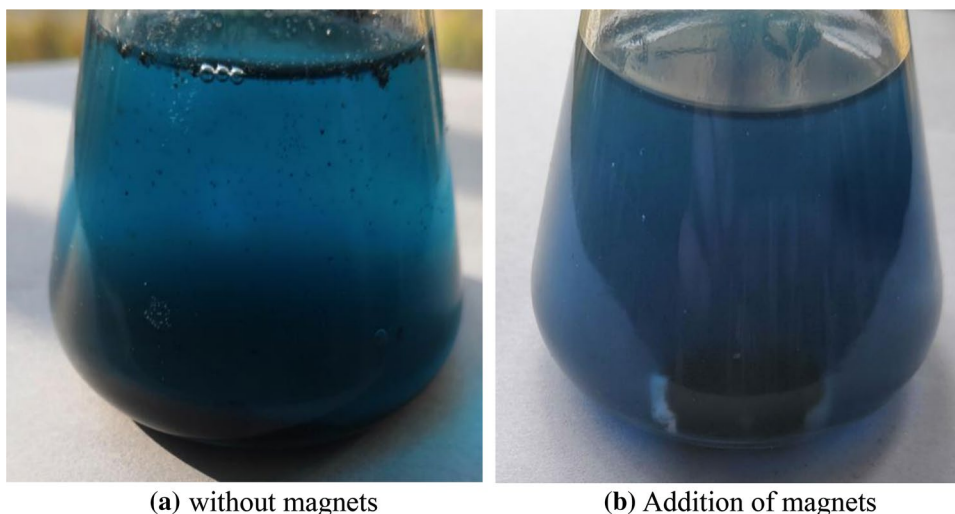
(a) without magnets   **(b)** Addition of magnets

Fig. 15 Adsorption isotherms of PAM/CA/Fe$_3$O$_4$ composite microspheres at different temperatures
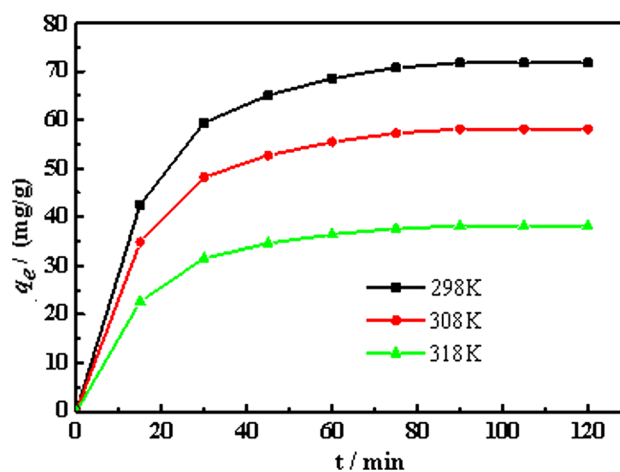

Fig. 16 Adsorption kinetics curves of PAM/CA/Fe$_3$O$_4$ magnetic composite microspheres at different temperatures

$$\frac{t}{q_t} = \frac{1}{K_2 q_e^2} + \frac{t}{q_e} \tag{7}$$

The q_e and q_t in the formula represent the equilibrium adsorption capacity and the adsorption capacity at the time t(min), respectively, mg/g; K_1 (1/min) and K_2 (g/mg min) were the kinetic constant of the quasi-first and quasi-second order, respectively. The fitting results of the two kinetic models are compared in Table 3. At different temperatures, the correlation coefficients of the quasi-first-order kinetic model of the microspheres are higher than those of the other model. It is indicated that the microspheres are more in line with the pseudo-first-order kinetic model, which indicates that the adsorption of microspheres is mainly based on surface adsorption. The calculated adsorption capacity is closer to the experimental value, which can better reflect the change of adsorption with time in the adsorption process (Fig. 16).

4 Conclusion

In this paper, a magnetic adsorption microsphere containing a metal–organic double network backbone was constructed by one-step method. The addition of Fe$_3$O$_4$ constructed the metal–organic double network skeleton structure on the basis of the double network through the coordination interaction of ligands with PAM and SA. Due to the coordination effect, the thermal stability of the microspheres was greatly improved, and the crystallinity of the microspheres was decreased. By constructing the skeleton structure, the specific surface area of the composite microspheres was greatly increased to 230 m^2/g. The surface area of the microsphere increased by 7 times compared with that without Fe$_3$O$_4$, and the size and distribution of the holes were also changed. It was found by SEM that a fibrous structure which is favorable

Table 2 Parameter table for fitting adsorption isotherms for different thermodynamic models

Temperature(K)	Langmuir adsorption isotherm			Freundlich adsorption isotherm		
	q_m (mg/g)	B (L/mg)	R^2	K_f (mg/g)	n	R^2
298	749.955	3.620×10^{-5}	0.9940	5.236×10^{-8}	0.0817	0.9960
308	723.883	1.149×10^{-6}	0.9930	5.419×10^{-14}	0.0528	0.9992
318	673.166	2.146×10^{-7}	0.9985	2.1×10^{-1}	0.0480	0.9989

Table 3 Parameter table obtained by fitting different kinetic models

Temperature (K)	q_e.exp (mg/g)	Pseudo-first-order kinetic model			Pseudo-second-order kinetic model		
		q_e (mg/g)	k_1 (1/min)	R^2	q_e (mg/g)	k_2 (g/mg min)	R^2
298	71.73	71.446	0.0588	0.9990	81.161	0.00101	0.9960
308	58.09	57.817	0.0596	0.9989	65.542	0.00128	0.9960
318	38.143	22.058	0.0409	0.9995	43.174	0.00190	0.9960

for adsorption was produced on the surface of the microsphere. When the amount of adsorbent was 0.1 g, the pH was 7 and the temperature was 25 °C, the adsorbent have the best adsorption capacity to MB and the maximum adsorption amount was 71.6 mg/g. The adsorption process satisfied the Freundlich thermodynamics and the quasi-first-order kinetic model. The adsorption was a multi-layer adsorption with both physical and chemical processes, and the temperature rise was not conducive to adsorption. After a number of adsorption–desorption cycles, it still had a high adsorption capacity. By adding Fe_3O_4 magnetic particles, the composite microspheres were easier to separate and recycle.

Compliance with Ethical Standards

Conflict of interest The authors declare no conflict of interest.

References

1. M. Amit, M. Akansha, B. Soumen et al., Graphitic carbon nitride (g-C_3N_4)-based metal-free photocatalysts for water splitting: a review. Carbon **149**, 693–721 (2019)
2. C.V. Reddy, I.N. Reddy, B. Akkinepally et al., Synthesis and photoelectrochemical water oxidation of (Y, Cu) codoped α-Fe2O3 nanostructure photoanode. J. Alloys Compds. **814**, 152349 (2020)
3. A. Mehta, A. Mishra, S. Basu et al., Band gap tuning and surface modification of carbon dots for sustainable environmental remediation and photocatalytic hydrogen production—a review. J. Environ. Manage. **250**, 109486 (2019)
4. X. Gong, M. Xin, M. Li et al., Preparation of magnetically responsive tea waste and it's adsorption of methylene blue from aqueous solution. Chem. Ind. Eng. Progr. **38**(2), 1113–1121 (2019)
5. P.D. Suhas, K.N. Sanna, N. Mallikarjuna et al., Membrane-based separation of potential emerging pollutants. Sep. Purif. Technol. **210**, 850–866 (2019)
6. A.S. Ibupoto, U.A. Qureshi, F. Ahmed et al., Reusable carbon nanofibers for efficient removal of Methylene Blue from aqueous solution. Chem. Eng. Res. Des. **136**, 744–752 (2018)
7. Y. He, D.B. Jiang, J. Chen et al., Synthesis of MnO_2 nanosheets on montmorillonite for oxidative degradation and adsorption of Methylene Blue. J. Colloid Interface Sci. **510**, 207–220 (2018)
8. D. Zhu, J. Xiao, L. Yang et al., Hydrothermal synthesis of MnO_2 and the structure-activity relationship of its adsorption of dye. Chem Ind Eng Progr **38**(8), 3774–3781 (2019)
9. N. Azbar, T. Yonar, K. Kestioglu, Comparison of various advanced oxidation processesand chemical treatment methods for COD and color removal from a polyester and acetate fiber dyein geffluent. Chemosphere **55**, 35–43 (2004)
10. E. Brillas, J.C. Calpe, J. Casado, Mineralization of 2, 4 -D by advanced electrochemical oxidation processes. Water Res. **34**, 2253–2262 (2000)
11. E. Brillas, B. Boye, M.A. Banos, J.C. Calpe et al., Electrochemical degradation ofchloropHenoxy and chlorobenzoic Herbicides in acidic aqueous medium by the Eroxi-coagulation method. Chemosphere **51**, 227–235 (2003)
12. U. Schumann, P. Grundler, Electrochemical degradation of organic substances at PbO2 anodes monitoring by continuous CO2 measurements. Wat. Res. **32**(9), 2835–2842 (1998)
13. T. Tohid, K. Mohammad, R. Mashallah et al., Textile waste, dyes/inorganic salts separation of cerium oxide-loaded loose nanofiltration polyethersulfone membranes. Chem. Eng. J. **385**, 123787 (2020)
14. V.R. Chandragiri, R. Neelakanta, A. Bhargav et al., Mn-doped ZrO_2 nanoparticles prepared by a template-free method for electrochemical energy storage and abatement of dye degradation. Ceram. Int. **45**, 15298–15306 (2019)
15. A. Ventura, G. Jacquet, A. Bermond et al., Electrochemical generation of the Fenton's reagent application to atrazine degradation. Water Res. **36**, 517–3522 (2002)
16. E.C. Liane-Lage et al., Molecular weight distribution of chlorolignin in bleached Kraft efluent by GPC and uhrafihration. Biresour. Technol. **68**, 63–70 (1999)
17. R.X. Yang, Research progress of source and treatment technology of heavy metal pollution in water. Resour. Conserv. Environ. Prot. **4**, 66 (2016). **(in Chinese)**
18. Z.L. Zang, X.L. Sun, Present situation and development of dye wastewater treatment technology. Chem. Eng. Des. Commun. **3**, 205 (2017). **(in Chinese)**
19. R.R. Kakarla, N. Kazuya, O. Tsuyoshi et al., Nanofifibrous TiO_2-core/conjugated polymer-sheath composites: synthesis, structural properties and photocatalytic activity. J. Nanosci. Nanotechnol. **10**, 7951–7957 (2010)
20. R.R. Kakarla, G.G. Vincent, H. Mahbub, Carbon functionalized TiO_2 nanofifibers for high efifficiency photocatalysis. Mater. Res. Exp. **1**, 015012 (2014)
21. R.S. Dassanayake, E. Rajakaruna, H. Moussa et al., One-pot synthesis of MnO_2-chitin hybrids for effective removal of Methylene Blue. Int. J. Biol. Macromol. **93**, 350–358 (2016)
22. F. Zhu, L.W. Li, J.D. Xing, Selective adsorption behavior of Cd(II) ion imprinted polymers synthesized by microwave-assisted inverse emulsion polymerization, adsorption performance and mechanism. J. Hazard. Mater. **321**, 103–110 (2017)
23. M.M. Ghobashy, A.E. Mohamed, pH-sensitive wax emulsion copolymerization with acrylamide hydrogel using gamma irradiation for dye removal. Radiat. Phys. Chem. **134**, 47–55 (2017)
24. N. Milosavljević, A. Debeljković, M.K. Krusić et al., Application of poly(acrlymide-co-sodium methacrylate) hydrogels in copper and cadmium removal from aqueous solution. Environ Prog. **33**, 824–834 (2014)
25. P. Liu, L.P. Jiang, L.X. Zhu et al., Synthesis of covalently crosslinked attapulgite/poly(acrylic acid-coacrylamide) nanocomposite hydrogels and their evaluation as adsorbent for heavy metal ions. J. Ind. Eng. Chem. **23**, 188–193 (2015)
26. Z.G. Li et al., Adsorption kinetics/thermodynamic behavior and adsorption/desorption mechanism of crystal violet by semi-interpenetrating sodium alginate/polyacrylamide hydrogel. J. Higher Educ. Chem. **5**, 2118–2127 (2017)
27. H. Zhang, T. Chen, H. Li et al., Preparation of polyacrylamide/calcium alginate composite microspheres adsorbent through emulsion polymerization. J. Dalian Polytech. Univ. **37**(5), 385–390 (2018)
28. S. Nethaji, A. Sivasamy, A.B. Mandal, Preparation and characterization of corn cob activated carbon coated with nano-sized

magnetite particles for the removal of Cr(VI). Biores. Technol. **134**(2), 94–100 (2013)

29. P. Hu, K. Chang, C. Zhenyu et al., Surface modification and application in biomedicine and environmental protection of magnetic Fe$_3$O$_4$ nanoparticles. Ciesc J. **68**(7), 2641–2652 (2017)

30. Y. Wenguang, T. Zhang, J. Zhang et al., The preparation methods of magnetite nanoparticles and their morphology. Progr. Chem. **06**, 884–892 (2007)

31. J. Yao, H. Wang, S. Gao et al., Adsorption of amaranth by betaine-modified Fe3O4 magnetic nanoparticles. J. Shanxi Univ. **42**(03), 611–618 (2019)

32. L. Huang, B. Li, Y. Yang et al., Preparation and characterization of β-cyclodextrin/Fe$_3$O$_4$ water-based magnetic fluid and its adsorption behavior for neutral red. Chin. J. Appl. Chem. **31**(05), 607–612 (2014)

33. Q. Wang, S. Zhu, W. Yang et al., (2017) Removal of Cr(VI) from aqueous solution by magnetic ferroferric oxide sodium alginate composite adsorbent. J. China West Normal Univ. **3**, 282–287 (2017)

34. X. Zou, H. Zhang, T. Chen et al., Preparation and characterization of polyacrylamide/sodium alginate microspheres and its adsorption of MB dye. Colloids Surf. A Physicochem. Eng. Asp. **567**, 184–192 (2019)

35. F. Wu, Y. Chen, J. Ma, Study on adsorption behavior of bamboo leaf powder on methylene blue dyes in wastewater. Anhui Chem. Ind. **45**(04), 33–36 (2019)

36. X. Zou, H. Zhang, T. Chen, Preparation and characterization of polyacrylamide/sodium alginate microspheres and its adsorption of MB dye. Colloids Surf. A **567**, 184–192 (2019)

37. L. Cui, X. Guo, Q. Wei et al., Removal of mercury and methylene blue from aqueous solution by xanthate functionalized magnetic graphene oxide: sorption kinetic and uptake mechanism. J. Colloid Interface Sci. **439**, 112–120 (2015)

38. L. Ren, J. Du, P. Zhai et al., Modification of polyurethane foam by carboxymethyl chitosan and its adsorption of methylene blue. J. Shanxi Univ. Sci. Technol. **37**(04), 6–10 (2019)

39. K. Jin, Z. Zhang, W. Zhang et al., Preparation of magnetic chitosan/diatomite composite and its adsorption of methylene blue. Liaoning Chem. Ind. **48**(08), 763–765 (2019)

40. S. Cui, Y. Zhang, Study on adsorption properties of methylene blue by grapefruit skin adsorbent. Chem. World **60**(07), 410–415 (2019)

41. N. Somsesta, V. Sricharoenchaikul, D. Aht-Ong, Adsorption removal of methylene blue onto activated carbon/cellulose biocomposite films: equilibrium and kinetic studies. Mater. Chem. Phys. **240**, 12221 (2020)

42. A.H. Jawad, R. Razuan, J.N. Appaturi et al., Adsorption and mechanism study for methylene blue dye removal with carbonized watermelon (*Citrullus lanatus*) rind prepared *via* one-step liquid phase H$_2$SO$_4$ activation. Surf. Interfaces **16**, 76–84 (2019)

43. Y. Tang, Y. Zhao, T. Lin et al., Adsorption performance and mechanism of methylene blue by H$_3$PO$_4$-modified corn stalks. J. Environ. Chem. Eng. (2019). https://doi.org/10.1016/j.jece.2019.103398

44. Q. He, Z. Li, C. Fu, Preparation of graphene oxide/diatomite composites and their application in the removal of methylene blue in wastewater. Chem. World **58**(5), 268–274 (2017)

45. X. Wang, G. Huang, G. Zhang et al., Preparation of magnetic crosslinking chitosan and adsorption of Th(IV) ions. New Chem. Mater. **39**(9), 66–69 (2011)

Junfeng Shi was born in Xingtai City, Hebei Province in 1994, graduated from Dalian Polytechnic University in 2018, and is now continuing his graduate studies at Dalian Polytechnic University.

Hong Zhang was born in Liaoyang, Liaoning Province, China in 1971. She received her PhD from Dalian University of Technology in 2008 and is now a professor at Dalian Polytechnic University.

Yue Yu was born in Dalian, Liaoning Province, China in 1982. She received her PhD from Peking University in 2011 and is now a professor at Dalian Polytechnic University.

Ming Yan was born in Changchun City, Jilin Province in 1997, graduated from Dalian Polytechnic University in 2019, and is now continuing his graduate studies at Dalian Polytechnic University.

Lingwei Liu was born in Wafang dian City, Liaoning Province in 1996, graduated from Dalian Polytechnic University in 2019, and is now continuing his graduate studies at Dalian Polytechnic University.

Haotong Zhu was born in Tieling City, Liaoning Province in 1997, graduated from Dalian Polytechnic University in 2018, and is now continuing his graduate studies at Dalian Polytechnic University.

Yongming Ye was born in Hefei City, Anhui Province in 1994, graduated from Dalian Polytechnic University in 2018, and is now continuing his graduate studies at Dalian Polytechnic University.

Yunhe Zhao was born in Tangshan City, Hebei Province in 1996, graduated from Dalian Polytechnic University in 2018, and is now continuing his graduate studies at Dalian Polytechnic University.

Jing Guo was born in Panjin, Liaoning Province, China in 1962. He received his PhD in Donghua University in 2008 and is currently a professor at Dalian Polytechnic University.